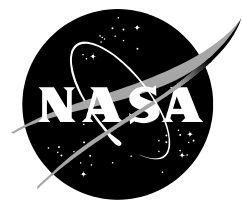NASA/TM—2020–220465

Fiber-Optic Strain-Based Deflection and Twist Sensing for a High-Aspect-Ratio Swept Wing

Francisco Pena
Armstrong Flight Research Center, Edwards, California

January 2020

NASA STI Program ... in Profile

Since its founding, NASA has been dedicated to the advancement of aeronautics and space science. The NASA scientific and technical information (STI) program plays a key part in helping NASA maintain this important role.

The NASA STI program operates under the auspices of the Agency Chief Information Officer. It collects, organizes, provides for archiving, and disseminates NASA's STI. The NASA STI program provides access to the NTRS Registered and its public interface, the NASA Technical Reports Server, thus providing one of the largest collections of aeronautical and space science STI in the world. Results are published in both non-NASA channels and by NASA in the NASA STI Report Series, which includes the following report types:

- TECHNICAL PUBLICATION. Reports of completed research or a major significant phase of research that present the results of NASA Programs and include extensive data or theoretical analysis. Includes compila-tions of significant scientific and technical data and information deemed to be of continuing reference value. NASA counter-part of peer-reviewed formal professional papers but has less stringent limitations on manuscript length and extent of graphic presentations.

- TECHNICAL MEMORANDUM. Scientific and technical findings that are preliminary or of specialized interest, e.g., quick release reports, working papers, and bibliographies that contain minimal annotation. Does not contain extensive analysis.

- CONTRACTOR REPORT. Scientific and technical findings by NASA-sponsored contractors and grantees.

- CONFERENCE PUBLICATION. Collected papers from scientific and technical conferences, symposia, seminars, or other meetings sponsored or co-sponsored by NASA.

- SPECIAL PUBLICATION. Scientific, technical, or historical information from NASA programs, projects, and missions, often concerned with subjects having substantial public interest.

- TECHNICAL TRANSLATION. English-language translations of foreign scientific and technical material pertinent to NASA's mission.

Specialized services also include organizing and publishing research results, distributing specialized research announcements and feeds, providing information desk and personal search support, and enabling data exchange services.

For more information about the NASA STI program, see the following:

- Access the NASA STI program home page at http://www.sti.nasa.gov

- E-mail your question to help@sti.nasa.gov

- Phone the NASA STI Information Desk at 757-864-9658

- Write to:
  NASA STI Information Desk
  Mail Stop 148
  NASA Langley Research Center
  Hampton, VA 23681-2199

NASA/TM—2020–220465
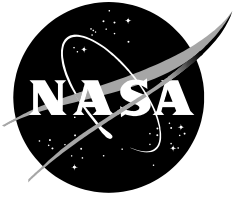
Fiber-Optic Strain-Based Deflection and Twist Sensing for a High-Aspect-Ratio Swept Wing

Francisco Pena
Armstrong Flight Research Center, Edwards, California

January 2020

Acknowledgments

This report is available in electronic form at

https://ntrs.nasa.gov

Abstract

Designs of aircraft structures have been moving toward leaner, lightweight designs for increased fuel efficiency. The Passive Aeroelastic Tailored (PAT) wing developed under the NASA Advanced Air Transport Technology (AATT) project is an example of a swept-wing design with high aspect ratio that incorporates lightweight highly-flexible tailored composite construction. The passive aeroelastic tailored structural design has explored the design space to enable aeroelastically tailored wing structures to increase aspect ratios (from 9 to 14) and ultimately reduce weight by 20 percent to 25 percent without impacting aeroelastic performance. To further study the aeroelastic performance of such a wing, the NASA Armstrong Flight Research Center (AFRC) (Edwards, California) has developed efficient real-time structural algorithms that are used in conjunction with a fiber-optic measurement system for lightweight vehicle applications. The AFRC Fiber Optic Sensing System (FOSS) provides up to 8,000 distributed surface strain measurements at one-half-inch increments and can be used to estimate a variety of structural parameters such as shape and load. This report discusses the implementation of strain-based displacement and twist-sensing techniques applied to the PAT wing test article tested at the NASA AFRC Flight Loads Laboratory. Empirical FOSS strain data are collected under varying loading conditions. Strain data are processed with the displacement and twist-sensing algorithms and independently verified by comparison to conventional ground-based instrumentation.

Nomenclature

A	area enclosed by the section median line, in^2
AFRC	Armstrong Flight Research Center
c	distance to bending neutral axis, in
$C\theta$	twist calibration coefficient, in^{-1}
DIC	digital image correlation
DTF	Displacement Transfer Function
E	elastic modulus, lbf-in^{-2}
FOSS	Fiber Optic Sensing System
FOSS-DTF	Displacement Transfer Function applied to FOSS strain data
FOSS-TTF	Twist Transfer Function applied to FOSS strain data
G	shear modulus, lbf-in^{-2}
h	structure height at sensing station, in
I	second moment of area, in^4
J	polar second moment of area, in^4
L	length between sensing stations, in
M	bending moment, in-lbf
NASA	National Aeronautics and Space Administration
PAT	Passive Aeroelastic Tailored (name of test article)
q	shear flow, lbf-in^{-1}
t	thickness, in
T	torque, in-lbf
TTF	Twist Transfer Function
w	load, lbf
X	forward and aft in aircraft coordinate frame
Y	right and left in aircraft coordinate frame
y	span distance of wing structure in local coordinate frame
Z	up and down in aircraft coordinate frame
α	surface strain orientation angle, deg
γ	shear strain, in/in

$\mathit{\Delta}$	difference
ε	normal strain, in/in
$\mathit{\Lambda}$	sweep angle, deg
θ	wing twist angle, aircraft pitch angle, deg
σ	normal stress, $\mathrm{lbf\text{-}in}^{-2}$
τ	shear stress, $\mathrm{lbf\text{-}in}^{-2}$
ϕ	wing slope angle, aircraft roll angle, deg
ψ	aircraft yaw angle, deg

Subscripts

A, B, C	reference sensor orientations for FOSS rosette
i, k	reference sensing station indices
u, l	reference to upper surface and lower surface
x, y, z	reference orthogonal orientations

Introduction

In June 2003, the National Aeronautics and Space Administration (NASA) experienced an in-flight structural breakup of the Helios Prototype airframe due to turbulence and excessive structural deflection. Among the technical recommendations and lessons learned was the need to develop a method for real-time measurement of the wing shape and methods to control aeroelastic divergence to avoid or reduce the risk of another such catastrophe (ref. 1). One method utilized previously at the NASA Armstrong Flight Research Center (AFRC) for in-flight monitoring of wing deflections is the electro-optical flight deflection measurement system (FDMS), which is composed of on-board cameras and several wing-mounted targets (ref. 2). The FDMS has been used on multiple vehicles such as the Highly Maneuverable Aircraft Technology (HiMAT) remotely piloted research vehicle (RPRV-870) (Rockwell International) (ref. 3), the X-29 forward-swept-wing Advanced Technology Demonstrator aircraft (Grumman Aerospace Corporation) (ref. 4), the Advanced Fighter Technology Integration (AFTI) F-111 Mission Adaptive Wing (MAW) research aircraft (General Dynamics Corporation) (GD) (ref. 5), the F-16C Block 40 aircraft (GD) (ref. 6) and the Active Aeroelastic Wing F/A-18 airplane (McDonnell Douglas, now The Boeing Company, Chicago, Illinois) (ref. 7).

This report presents an alternative approach to obtaining real-time in-flight monitoring of wing deformation, utilizing fiber-optic sensing embedded with multiple fiber Bragg gratings (FBGs) along with strain-based deflection and twist algorithms. The fiber-optic sensors are lightweight, thin (approximately the diameter of a human hair) (ref. 8), flexible, easily applied to exterior surfaces, and may be multiplexed, allowing real-time access to distributed strain data. The Fiber Optic Sensing System (FOSS) utilized to obtain the data presented in this report was developed at the NASA AFRC. The FOSS can be used to interrogate optical fiber with a series (up to 1,000) of distributed FBGs to provide real-time strain data (ref. 8). During testing of wing structures, the FOSS can simultaneously and continuously interrogate eight 40-ft optical fibers containing FBGs at one-half-inch intervals, providing nearly 8,000 strain sensor readings per scan at 20 Hz in this application. The FOSS can provide 100 times the number of strain measurements at 1/100th the total sensor weight when compared to conventional electrical-resistance strain gage implementations in a sensor-to-sensor comparison (ref. 8). The FOSS can operate in stand-alone mode, which is used for flight applications, or in remote control mode, in which a laptop is connected to provide monitoring and control. A centralized software interface combines all functions into a suite of applications to interface with FOSS data. The high spatial density of the FBGs has enabled engineers to develop strain-based shape-estimation algorithms.

These shape-estimation algorithms are known as the Displacement Transfer Function (DTF) and Twist Transfer Function (TTF). The DTF and TTF calculations can be utilized independently from the FOSS, though the FOSS is an ideal and practical system for providing distributed strain measurements. Herein, when the DTF is paired with FOSS data, the resulting calculation is referred to as the FOSS-DTF,

and when the TTF is paired with FOSS data, the resulting calculation is referred to as the FOSS-TTF. The FOSS-DTF has been implemented on various flight-test articles and flown on vehicles such as the modified General Atomics (San Diego, California) Predator B (Ikhana) vehicle (ref. 8), the AeroVironment, Incorporated (Monrovia, California) Global Observer unmanned aircraft (refs. 8, 9), the X-56 Multi-Utility Technology Testbed (MUTT) aircraft (Lockheed Martin, Bethesda, Maryland) (ref. 10), and the RnR Products (Milpitas, California) Alternatively Piloted Vehicle (APV-3) small unmanned research aircraft (ref. 11). Such methods have the potential for use in structural health monitoring (SHM) and flight control.

Strain-Based Shape-Sensing Algorithm

The typical local coordinate frame for an aircraft defines the local X-axis to be aligned forward and aft, and the rotation about the X-axis is referred to as the roll angle, defined as ϕ. The change in slope of the aircraft wing structure due to structural deformation will also be defined as ϕ. Orthogonal to the local aircraft X-axis and on the horizontal plane of reference is the local aircraft Y-axis which is aligned left and right, and the rotation about the Y-axis is referred to as the pitch angle and is defined as θ. In this report, the change in pitch of the aircraft wing structure will also be referred to as twist angle and will also be defined as θ. The local aircraft Z-axis is aligned vertically in the up and down direction, and a rotation about the Z-axis will be referred to as the yaw angle and is defined as ψ. An illustration of a typical aircraft local coordinate system frame is shown in figure 1.
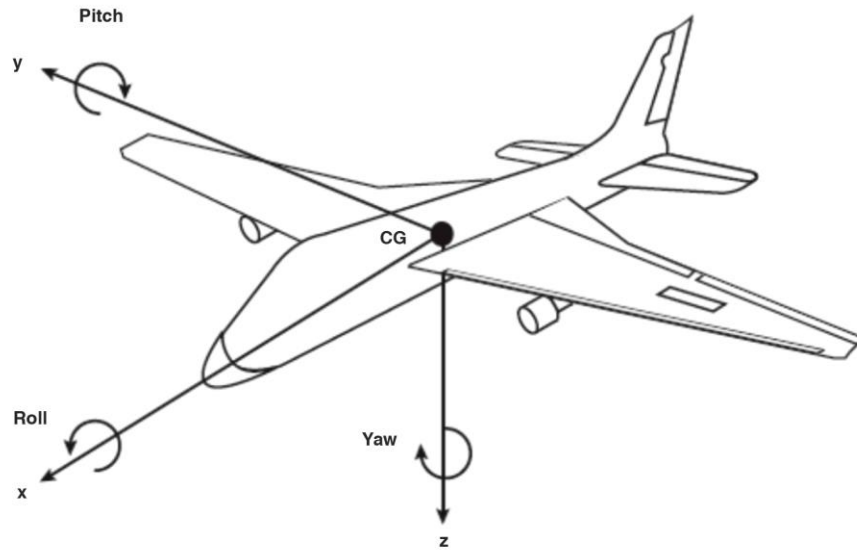
Figure 1. Aircraft local coordinate system frame.

The strain-based shape-prediction algorithm, also known as the DTF, is derived from classical beam theory (Euler-Bernoulli) for several beam configurations including cantilever beams, which are analogous to the wing spar structure in aircraft. The classical beam theory can be used to relate the loading of a structure to the theoretical curvature, slope, and deflection of a cantilever beam. The general differential equation that describes the relationship between a loading function and the resulting shape of a beam is shown in equation (1) (ref. 12):

$$\frac{d^4 z(y)}{dy^4} = \frac{w(y)}{E(y)I(y)} \tag{1}$$

3

where the variable y is the span distance of the structure starting at the wing root and ending at the end of the beam, $z(y)$ is the vertical displacement of a beam as a function of distance from the root, $w(y)$ is the loading function analogous to the lift generated by the wing, E is the elastic modulus, and I is the second moment of area that is calculated with respect to the centroidal axis perpendicular to the applied loading. For the purposes of implementing the strain-based shape-estimation algorithm, the equation of interest is the moment-strain relationship of the classical beam differential equation which states that the curvature, which is the second derivative of displacement $z(y)$ of a beam, is proportional to the applied bending moment $M(y)$, as shown in equation (2) (ref. 12):

$$\frac{d^2z(y)}{dy^2} = \frac{M(y)}{I(y)E(y)} \tag{2}$$

Bending moment cannot be measured directly, so strain gages are placed on the upper and lower surfaces and utilized to quantify the bending moments. The bending stress on the upper surface and the normal stress $\sigma_u(y)$ can be related to strain $\varepsilon_u(y)$, as shown in equation (3):

$$\sigma_u(y) = \frac{M(y)c_u(y)}{I(y)} = E(y)\varepsilon_u(y) \tag{3}$$

where ε_u is the strain measurement on the upper surface and c_u is the vertical distance to the neutral axis from the upper surface. The neutral axis is a horizontal axis where the bending moment is equal to zero at a given span location. Rearranging terms as in equation (4) shows that:

$$\frac{M(y)}{I(y)E(y)} = \frac{\varepsilon_u(y)}{c_u(y)} \tag{4}$$

An illustration of the neutral axis is provided in figure 2.
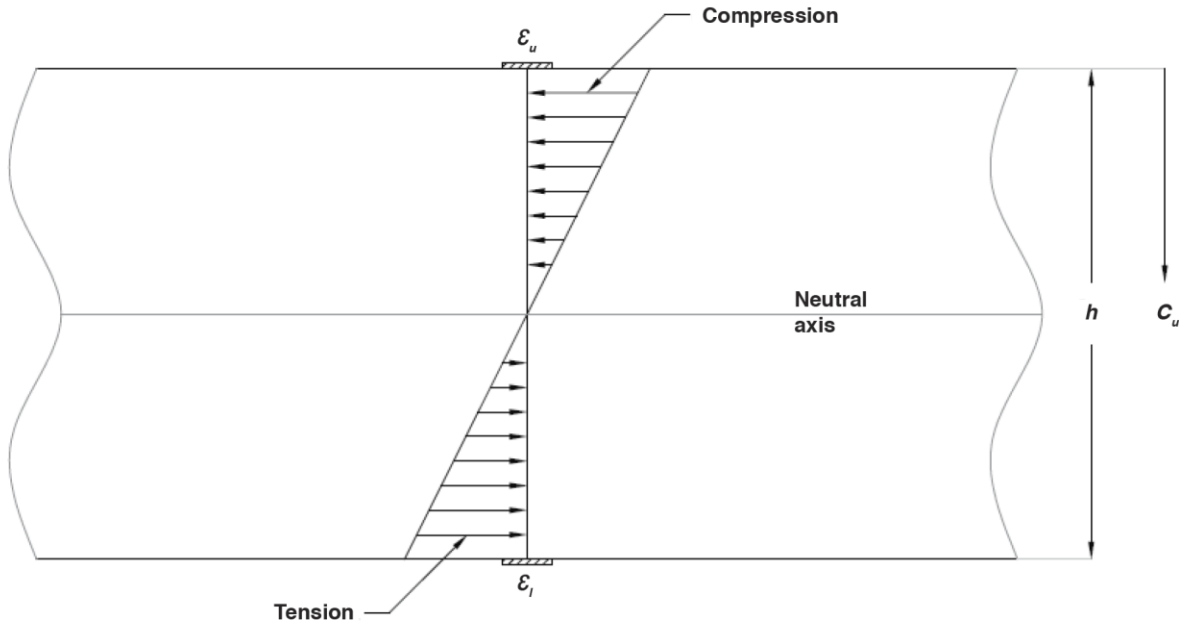
Figure 2. Example of neutral axis distance.

As stated by Bakalyar (ref. 13), the distance to the neutral axis from the upper surface can be found experimentally by assuming a linear stress/strain distribution from the upper surface (ε_u) to the lower surface (ε_l). A pair of strain measurements placed on the upper and lower surfaces at the same span location can be utilized to find the distance to the neutral axis, as shown in equation (5):

$$c_u(y) = \frac{h(y)\varepsilon_u(y)}{\varepsilon_l(y) - \varepsilon_u(y)} \tag{5}$$

where h is the height difference between the upper and lower surface strain measurements. Combining the Euler-Bernoulli beam curvature equation in equation (2) with equation (4) and equation (5), Ko, Richards, and Tran (ref. 14) showed that the Euler-Bernoulli curvature equation can be expressed as the measured strain and geometry of a structure, as shown in equation (6).

$$\frac{d^2z(y)}{dy^2} = \frac{\varepsilon_l(y) - \varepsilon_u(y)}{h(y)} \tag{6}$$

The Euler-Bernoulli beam curvature equation is approximately equal to the incremental change in slope (in a local structural coordinate frame) over the strain-sensing distance, and is expressed as shown in equation (7):

$$\frac{d^2z(y)}{dy^2} = \frac{d\,(\tan(\phi))\,(y)}{dy} \approx \frac{d\phi(y)}{dy} \approx \frac{\Delta\phi_i}{\Delta L} \tag{7}$$

where $\tan(\phi) \approx \phi$ for small angles (angles less than 9 deg), $\Delta\phi_i$ is the incremental slope change over the i_{th} sensing element, and ΔL is the distance between the sensor stations (see figure 3). With these approximations, the shape-sensing algorithm no longer requires the shape calculations to be a continuous function of y along the span of the structure, but rather can be treated as discrete nodal points and sensing elements. Forward kinematic equations utilizing joint angles and rigid links (see figure 4) can be utilized to calculate the distributed shape. By combining the elemental slope change approximations in equation (7) and the strain-based curvature equation defined in equation (6), the incremental elemental change in slope in between adjacent node stations can be calculated as shown in equation (8).
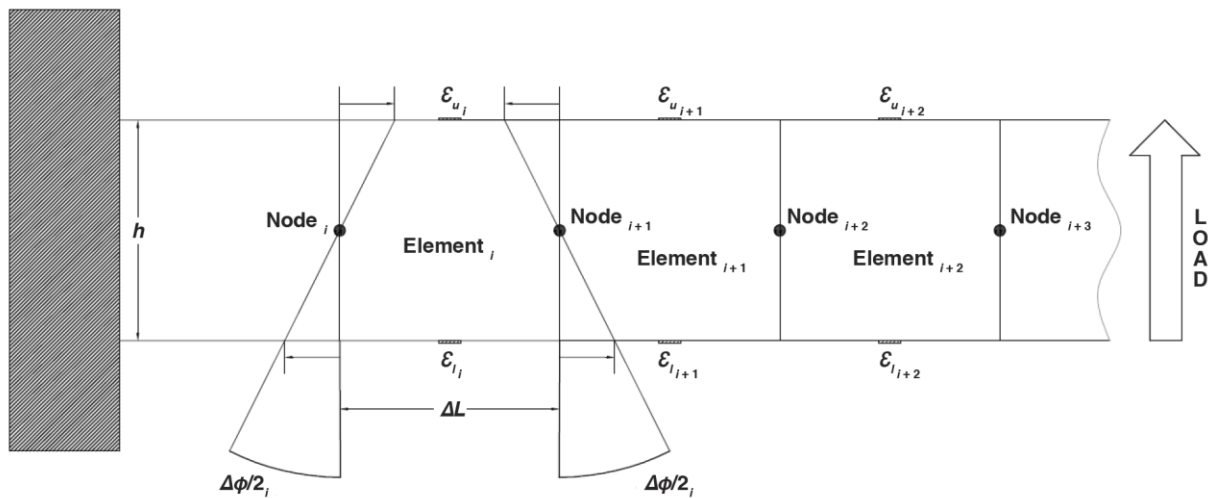
Figure 3. Illustration of nodal points and sensing elements.
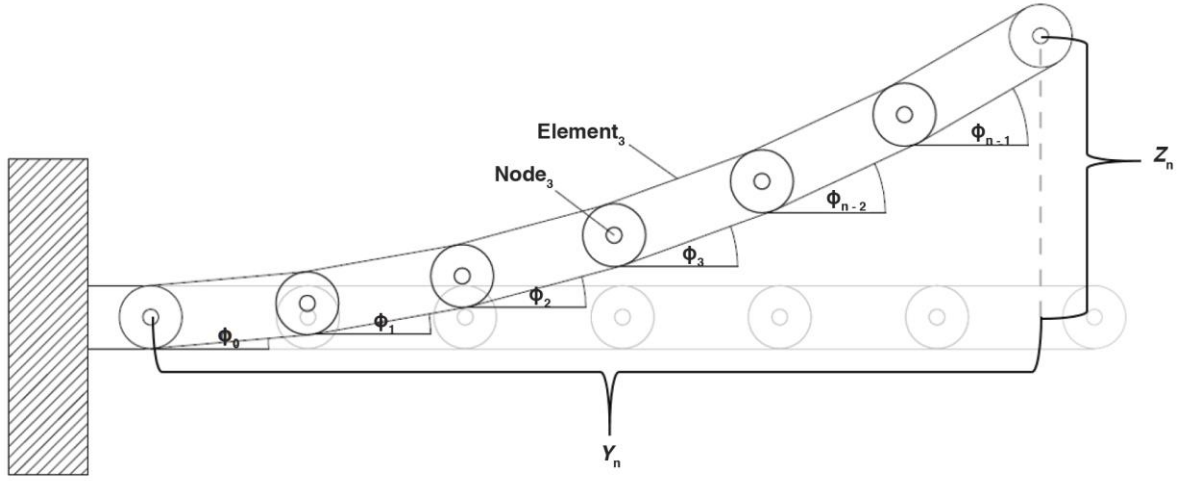
Figure 4. Example of forward kinematic chain for vertical displacement.

$$\Delta\phi_i = \frac{\varepsilon_{l_i} - \varepsilon_{u_i}}{h_i} \Delta L_i \tag{8}$$

The distributed slope profile of the structure can be found by summing the elemental slope changes as shown in equation (9):

$$\phi_n = \phi_0 + \sum_{i=1}^{n} \Delta\phi_i \tag{9}$$

where ϕ_0 is the initial root slope condition. The vertical displacement (Z_n) and lateral position (Y_n) at each node can be approximated by utilizing trigonometric functions. The process of determining the vertical displacement at any nodal station n is called the DTF. The DTF can be determined by summing the sine of the slope angle ϕ_i multiplied by the sensor station spacing ΔL as shown in equation (10) with reference to figure 4.

$$Z_n = Z_0 + \sum_{i=1}^{n} sin(\phi_i)\Delta L_i \tag{10}$$

The horizontal position (Y_n) of each discrete nodal station can be approximated by summing the cosine of the slope angle ϕ_i multiplied by the sensor station spacing ΔL as shown in equation (11):

$$Y_n = Y_0 + \sum_{i=1}^{n} cos(\phi_i)\,\Delta L_i \tag{11}$$

While in flight, the twist of a wing results in a change in the local angle of attack of the two-dimensional cross-section, which in turn changes the lift profile over the wing. A flexible wing may have the strength to carry the gross weight of a vehicle, but could be susceptible to aeroelastic divergence

6

given enough deformation. To measure the twist of a wing in real time, a strain-based twist-sensing method has been developed. The angle of twist of a structure can be calculated by utilizing equation (12) (ref. 12):

$$\theta(y) = \frac{T(y)L(y)}{G(y)J(y)} \quad \longrightarrow \quad \Delta\theta_k = \frac{T_k \Delta L_k}{G_k J_k} \tag{12}$$

where $\Delta\theta_k$ is the incremental kth element change in twist angle between adjacent sensing stations, ΔL_k is the distance between shear-strain-sensing stations, T_k is the total torque at the given element cross-section, G_k is the material shear modulus and J_k is the polar second moment of area. The torque cannot be measured directly, so strain gage rosettes are used to measure shear strain. Strain rosettes are a group of three individual strain gages (ε_A, ε_B, ε_C), with unique orientations ($\alpha_A, \alpha_B, \alpha_C$), see figure 5. Three unique orientations, as shown in equation (13), are required in order to solve for three strain components: the normal strain in the X-axis (ε_x), normal strain in the Y-Axis (ε_y), and the shear strain relative to the X and Y axis. (γ_{xy}).
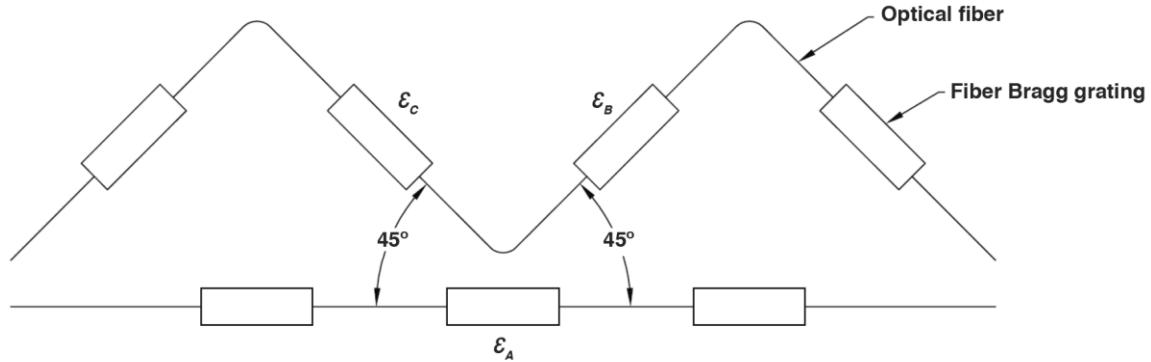

Figure 5. Example of a FOSS rosette used on the CREW test article.

$$\begin{bmatrix} \varepsilon_A \\ \varepsilon_B \\ \varepsilon_C \end{bmatrix} = \begin{bmatrix} \cos^2 \alpha_A + \sin^2 \alpha_A + \sin \alpha_A \cdot \cos \alpha_A \\ \cos^2 \alpha_B + \sin^2 \alpha_B + \sin \alpha_B \cdot \cos \alpha_B \\ \cos^2 \alpha_C + \sin^2 \alpha_C + \sin \alpha_C \cdot \cos \alpha_C \end{bmatrix} \cdot \begin{bmatrix} \varepsilon_x \\ \varepsilon_y \\ \gamma_{xy} \end{bmatrix} \tag{13}$$

The torque can be related to shear strain as shown in equation (14):

$$\left. \begin{array}{l} T_k = 2A_k q_k \\ q_k = \tau_{xy_k} t_k \\ \tau_{xy_k} = G_k \gamma_{xy_k} \end{array} \right\} \quad \longrightarrow \quad T_k = 2A_k G_k t_k \gamma_{xy_k} \tag{14}$$

where A is the area enclosed by the section median line, q is the shear flow through an enclosed cell, t is the wall thickness, τ_{xy} is the shear stress on the surface of the structure and γ_{xy} is the shear strain on the surface of the structure. This method requires that shear-strain measurements be obtained by strain gages placed on the outer mold line, on the upper and lower surfaces and not on the vertical webs, to avoid coupling shear flow from adjacent cells as shown in figure 6, and also to avoid coupling from shear stress due to vertical and bending loads.
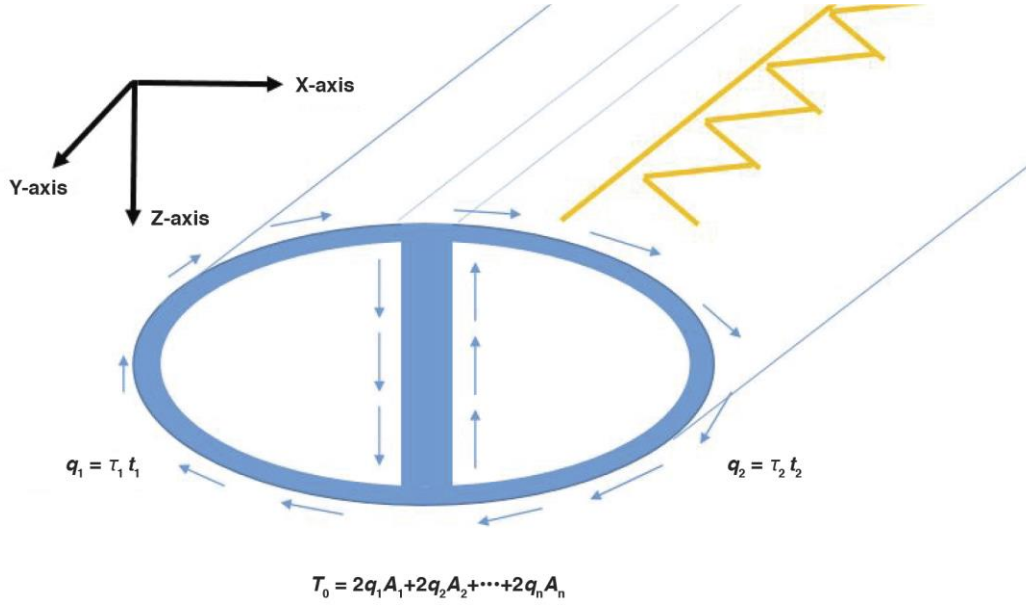
Figure 6. Example of cross section shear flow from torque in multi-celled structure.

The incremental change in twist angle over the element can be related to shear strain by combining the terms from equation (12) and equation (14) to yield equation (15):

$$\Delta\theta_k = \frac{2A_k t_k}{J_k}\gamma_{xy_k}\Delta L_k \tag{15}$$

It is possible to experimentally determine the combined effect of the second moment of area (J), wall thickness (t) and area enclosed by the section median line (A) by solving for a twist calibration term (C_{θ_k}). The twist calibration term (C_{θ_k}) can be defined as shown in equation (16):

$$C_{\theta_k} = \frac{2A_k t_k}{J_k} \tag{16}$$

where the calibration term has units of inverse length and can be experimentally found by applying a torque to the structure and measuring the shear-strain response (γ_{xy_k}) from the FOSS and the deformed twist angle response ($\Delta\theta_k$) from an independent measurement system. The difference between the twist angles between two node stations compared to the elemental shear strain measured between the stations can be correlated as shown in equation (17).

$$C_{\theta_k} = \frac{\Delta\theta_k}{\gamma_{xy_k}\Delta L_k} \tag{17}$$

Once the calibration coefficient is obtained, it can be multiplied by the shear strain and sensing distance to estimate the elemental change in twist angle, as shown in equation (18).

$$\Delta\theta_k = C_{\theta_k}\gamma_{xy_k}\Delta L_k \tag{18}$$

An illustration of the relationship between shear strain and twist angle can be found in figure 7.

8
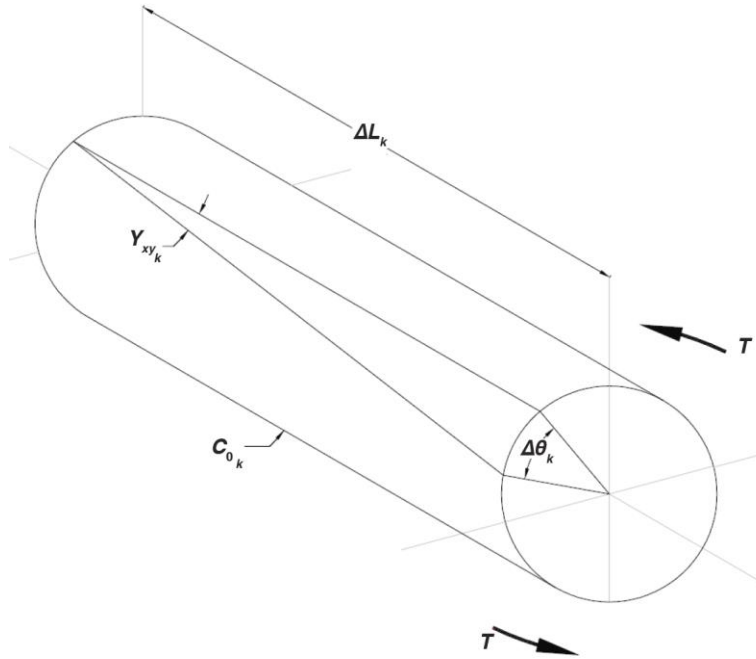
Figure 7. Illustration of shear strain to twist angle relationship.

The process of determining the twist angle at any nodal station m is the TTF and can be determined by summing the incremental twist contributions at each element using equation (19):

$$\theta_m = \theta_0 + \sum_{k=1}^{m} \Delta\theta_k \tag{19}$$

Test Article Description

The Passive Aeroelastic Tailored (PAT) wing test article is a carbon-epoxy, semi-span, right wingbox which was designed and manufactured by Aurora Flight Sciences (Dayton, Ohio) using a newer composite technology known as tow-steering fibers. The test article, shown in figure 8, is a 27-percent scale model of the undeflected Common Research Model (uCRM) with a high aspect ratio of 13.5, a 36.8-deg wing sweep, and a span of approximately 39 ft from the leading edge (LE) root to the trailing edge (TE) tip.
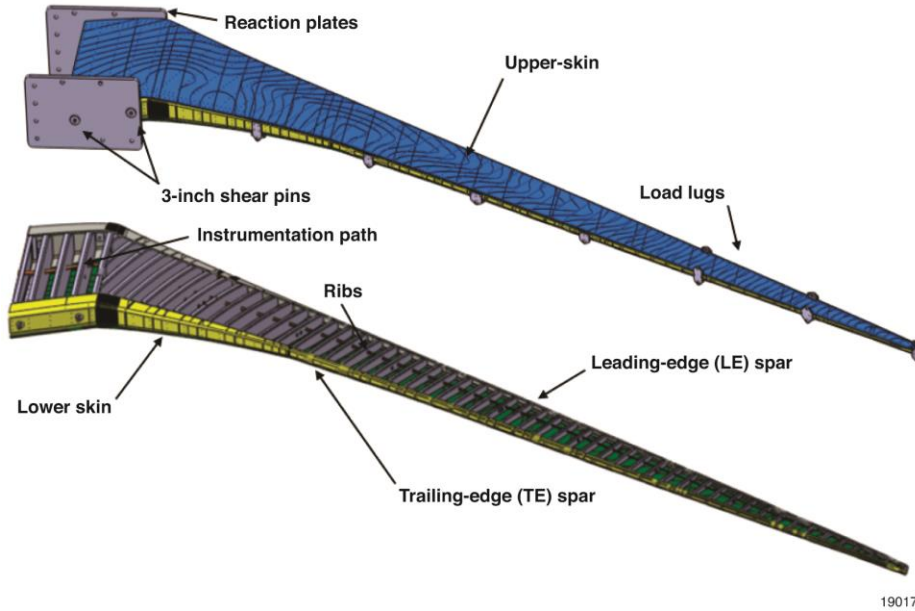
Figure 8. The Passive Aeroelastic Tailored wing test article.

Test Setup Description

The test article was cantilevered from a self-reacting wing loads test fixture, where the load trains push off of the test fixture while the test fixture also simultaneously constrains the wing. Four aircraft pins were used to secure the wing spars to a simulated wingbox, which was mounted to the self-reacting wing loads test fixture (see figure 9 and figure 10). Load was applied to the wing using a system of 14 load trains for the download Design Limit Loads (DLL) cases and flexural test. Each load train included a hydraulic actuator, force transducer, and clevis. The load trains were designed to provide an upload or download to the wing. Due to the large vertical displacements during the upload DLL load cases, the test utilized an overhead structure for applying loads. The overhead structure contained three actuators attached to a whiffletree structure that attached to the wing lugs.
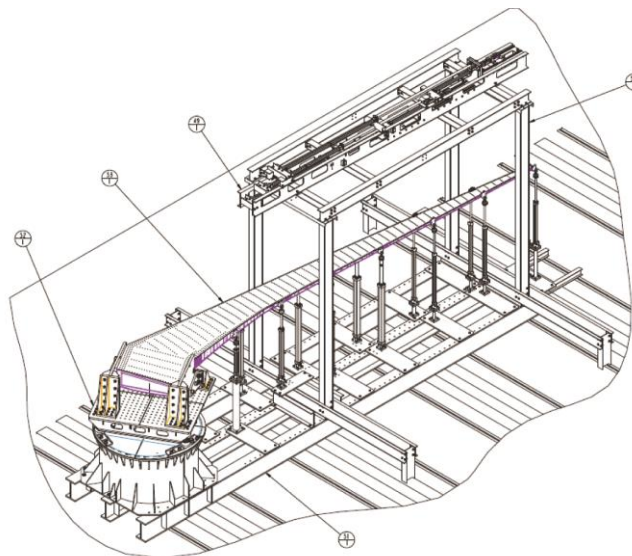

Figure 9. The load train setup under the test wing.

Figure 10. The test setup for the Passive Aeroelastic Tailored wing.

Instrumentation

The PAT wing was instrumented with various types of instrumentation to characterize the structural response to applied load. Instrumentation included measurements of strain, displacement, angles and applied load. Load cells were installed between the load-train-to-wing interface to monitor input loads to the wing. Wing displacement measurements were made using displacement transducers, including string potentiometers and linear variable differential transducers. Wing-twist-angle and slope-angle measurements were made using dual-axis inclinometers. In addition, a digital image correlation (DIC) system was utilized to estimate displacements and twist angles through digital image processing, by tracking the movements of targets placed on the wing. The FOSS-DTF vertical deflection estimates are compared against string potentiometers and displacement output of the DIC system. The FOSS-TTF twist estimates are compared against inclinometers and twist calculations from the DIC system.

The wing test article was instrumented with eight 40-ft sensing optical fibers with one-half-inch-spaced FBGs containing 1,000 strain sensors per fiber. Optical sensing fibers were bonded to the upper and lower surfaces along the forward and aft spar. Two optical sensing fibers were also placed at the 40-percent chord on the upper and lower surfaces. On the upper and lower surfaces, an optical sensing fiber was installed offset approximately four inches from the leading spar and routed in a $\pm$ 45-deg pattern spaced four rib bays apart. Figure 11 and figure 12 show the layout of the optical sensing fibers on the PAT wing. The intent of the pattern was to create a 0-deg / +45-deg / -45-deg rosette pattern similar to the pattern illustration in figure 5.
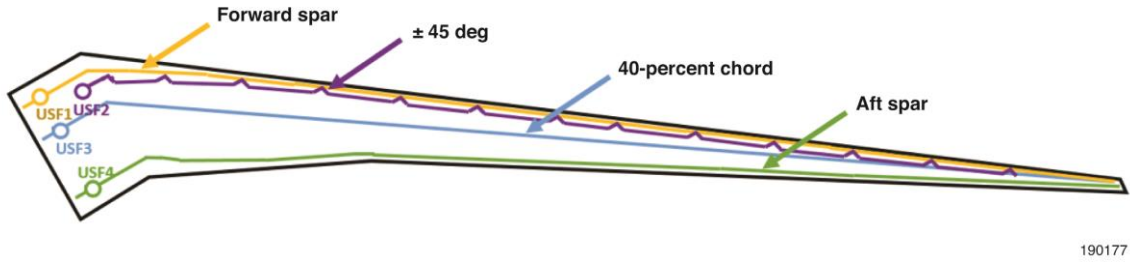
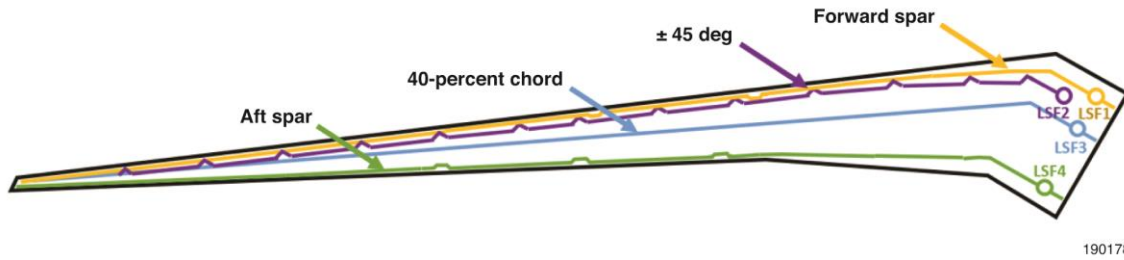Figure 11. The FOSS layout sketch on the upper surface of the wing test article.

Figure 12. The FOSS layout sketch on the lower surface of the wing test article.

In this report, the sensing fibers installed on the upper and lower surface of the forward spar (the yellow curve shown in figure 11 and figure 12) are used with the DTF to calculate vertical displacement. The ±45-deg zig-zag pattern (the purple curve shown in figure 11 and figure 12) intersection with the forward-spar sensing fiber is used as inputs to the strain rosette transform (eq. (13)) to calculate shear strain (γ_{xy_k}). The calculated shear strain is used with the TTF to calculate twist over 13 shear-strain-sensing elements.

Load Case Description

The PAT wing loads test included 17 load cases which were broken down into eight single-point flex-axis tests (two cycles each), four distributed negative-g loads tests, and five distributed positive-g loads tests. The download tests were broken down into incremental steps leading to 100-percent download DLL, ranging from 25 percent, 50 percent, 75 percent, and 100 percent. The upload tests were broken down into incremental steps leading to 90 percent upload DLL, ranging from 25 percent, 50 percent, 75 percent, 80 percent, and 90 percent.

Displacement Transfer Function Test Results

The FOSS strain data recorded at the time of maximum vertical deflection of 90-percent upload DLL are shown in figure 13. Also included in the figure are the metallic foil strain gages which were installed adjacent to the FOSS sensing fibers. The 90-percent upload DLL is provided as the example load case because it has the largest vertical deflection and has the largest difference between the FOSS-DTF and string potentiometer. The FOSS strain data were utilized with the modified Euler-Bernoulli beam equation (equation (8)) to determine the incremental change in slope $\Delta\phi_i$ at each i_{th} strain-sensing station. It should be noted that the curvature calculations are in a local coordinate frame aligned along the forward spar orientation, which is swept aft relative to the global aircraft coordinate system. The vertical deflection at the wing tip is not affected by the choice of a local coordinate frame or global coordinate frame. It is also noted that the wing slope in this section is also in the local coordinate frame.

12
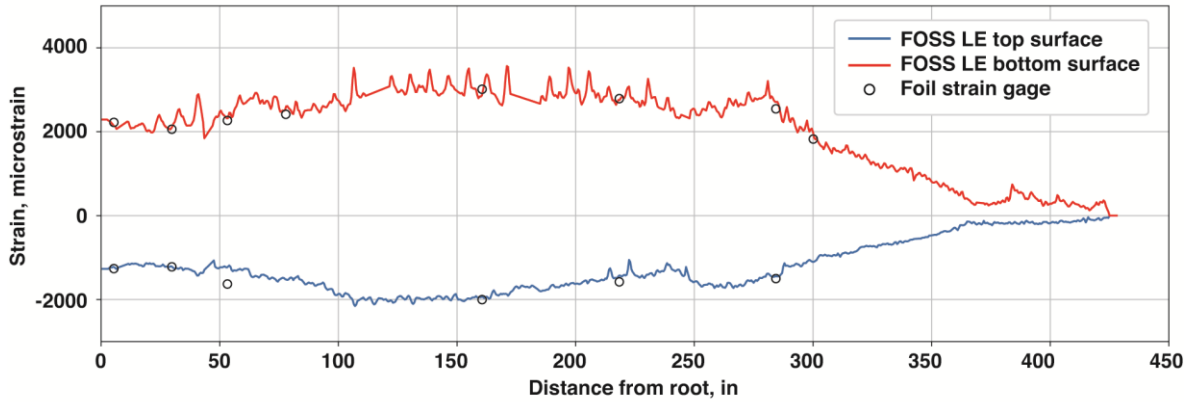
190179

Figure 13. Load case 90-percent upload DLL, strain distribution on top and bottom surface of forward spar, and foil strain gages (local coordinate frame).

The output of the incremental slope change equation (equation (8)) was then utilized in the distributed slope equation (equation (9)) to calculate the slope ϕ_i of the structure at each i_{th} sensing station. The incremental change in slope is shown in figure 14.
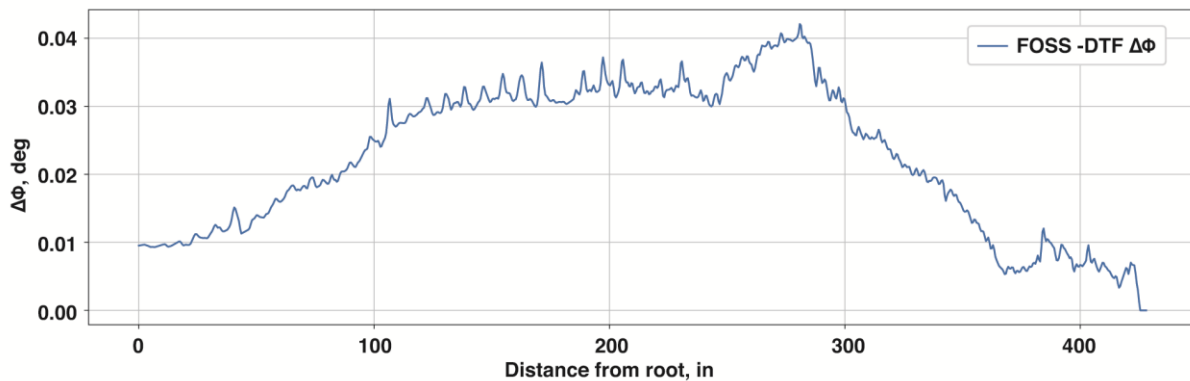
190180

Figure 14. Load case 90-percent upload DLL, FOSS-DTF incremental slope change (local coordinate frame).

The structure being pinned at the root, the initial slope ϕ_0 is predicted to be non-zero. To account for the non-zero root slope, a calibration of root-bending strain to root rotation was performed. An inclinometer at the root of the wing provided an estimate for the root rotation, and the root-bending strain was calculated by utilizing the difference in strain on the top and the bottom surfaces at the root of the test article. The root-bending strain obtained by the FOSS was multiplied by a calibration factor to provide a strain-based estimation for the root rotation. The root rotation calibration was utilized in all load cases presented in this report. The FOSS-DTF calculated slope (deg) from root to wing tip, along with nine distributed inclinometer readings, are plotted in figure 15.

13
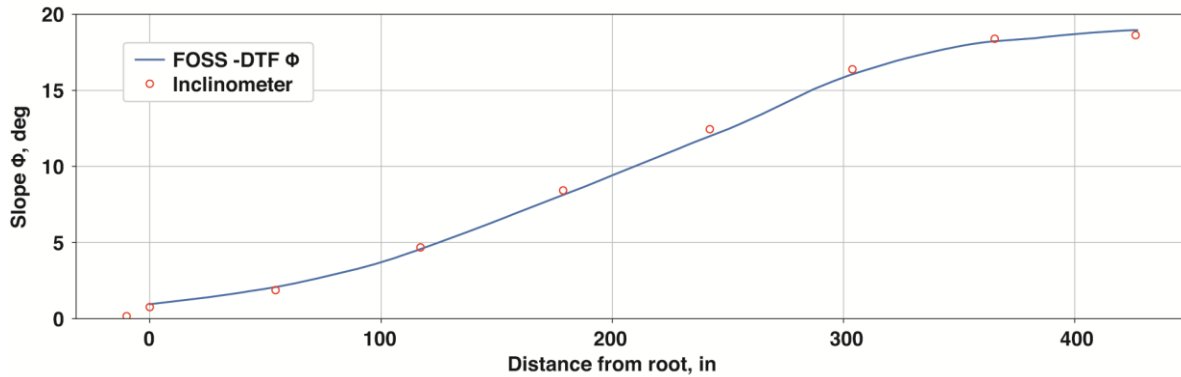
190181

Figure 15. Load case 90-percent upload DLL, FOSS-DTF distributed slope angle calculation and inclinometers (local coordinate frame).

The calculated distributed slope (eq. (9)) was then applied to the forward kinematic chain equation (eq. (10)) to calculate the vertical deflection. The resulting FOSS-DTF displacement calculation, eight string potentiometer readings, and DIC results for Load case 90-percent upload DLL are shown in figure 16.
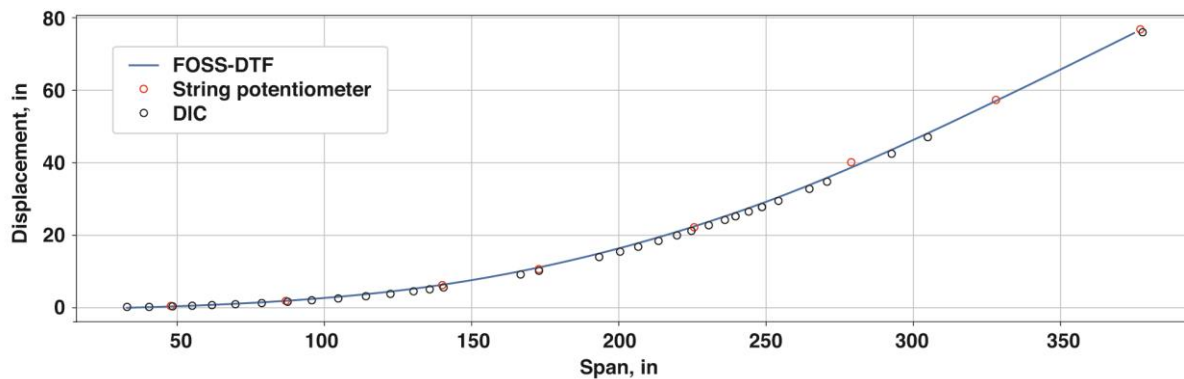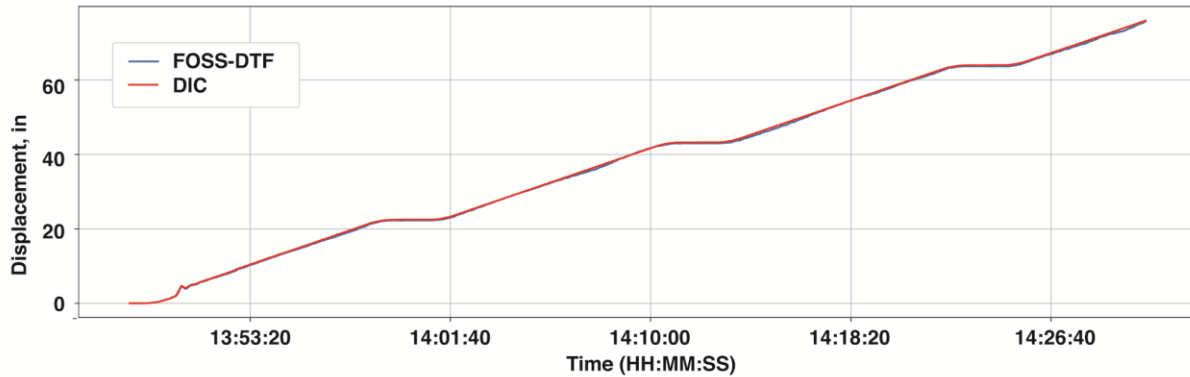

190182

Figure 16. Load case 90-percent upload DLL, FOSS-DTF vertical deflection calculation, string potentiometers and DIC (global coordinate frame).

At the maximum vertical deflection, the string potentiometer and FOSS-DTF were in close agreement, with a maximum difference of 1.63 percent. The string potentiometer recorded a maximum deflection of 76.79 in while the FOSS-DTF calculated 76.11 in.

At the maximum vertical deflection, the DIC and FOSS-DTF were in close agreement, with a maximum difference of 0.6 percent. The DIC recorded 75.99 in at the outboard target while the adjacent FOSS-DTF location calculated 76.11 in.

The time history of the DIC and FOSS-DTF wing-tip displacement for Load case 90-percent upload DLL is shown in figure 17. The time history of the difference between FOSS-DTF and DIC is shown in figure 18.

14

190183

Figure 17. Load case 90-percent upload DLL wing-tip displacement time history, FOSS-DTF and DIC.
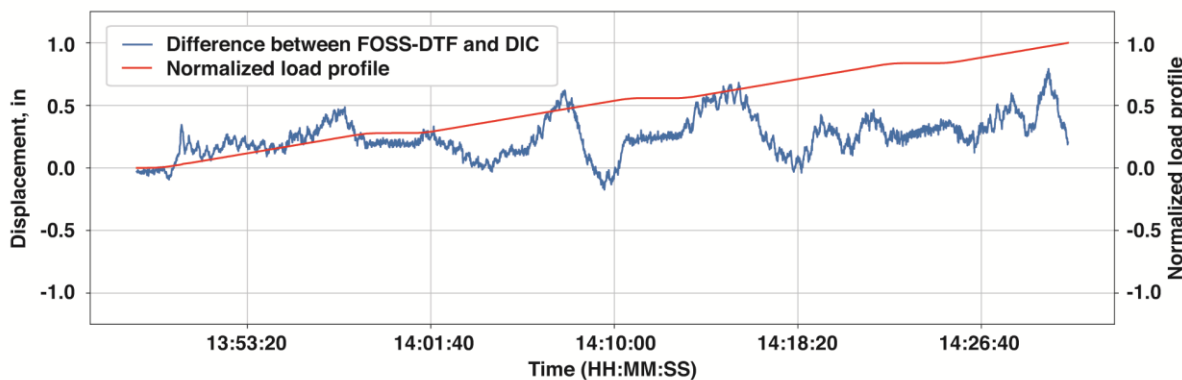
190184

Figure 18. Load case 90-percent upload DLL time history of difference in wing-tip displacement between FOSS-DTF and DIC, and normalized load profile.

The mean difference from the FOSS-DTF and DIC for Load case 90-percent upload DLL is 0.09 in, the standard deviation is 0.15 in, and the maximum difference is 0.48 in. An equivalent analysis was performed for the outboard string potentiometer and the adjacent FOSS-DTF calculation. The mean difference from the FOSS-DTF and outboard string potentiometer for Load case 90-percent upload DLL is 0.39 in, the standard deviation is 0.25 in, and the maximum difference is 1.25 in.

A summary of the remaining load cases is shown in figure 19. Over all the load case profiles, the maximum difference between the DIC and FOSS-DTF occurred during the Flex Axis TE Station 5, Cycle #1 with a difference of 0.95 in (excluding the 75-percent Upload test case, where test conditions exceeded the FOSS operational strain range settings during this test sequence). An equivalent analysis was performed for the outboard string potentiometer and the adjacent FOSS-DTF calculation. Over all the load case profiles, the maximum difference between the string potentiometer and FOSS-DTF is 1.77 in during the 80-percent Upload DLL test case. Compared to the string potentiometers, it is assumed that the DIC deflection results are closer to the true deflection of the PAT wing, especially during large deformations, since the string potentiometer cannot distinguish lateral (inboard or outboard) displacements from vertical displacements. String potentiometers thus tend to overestimate displacements.
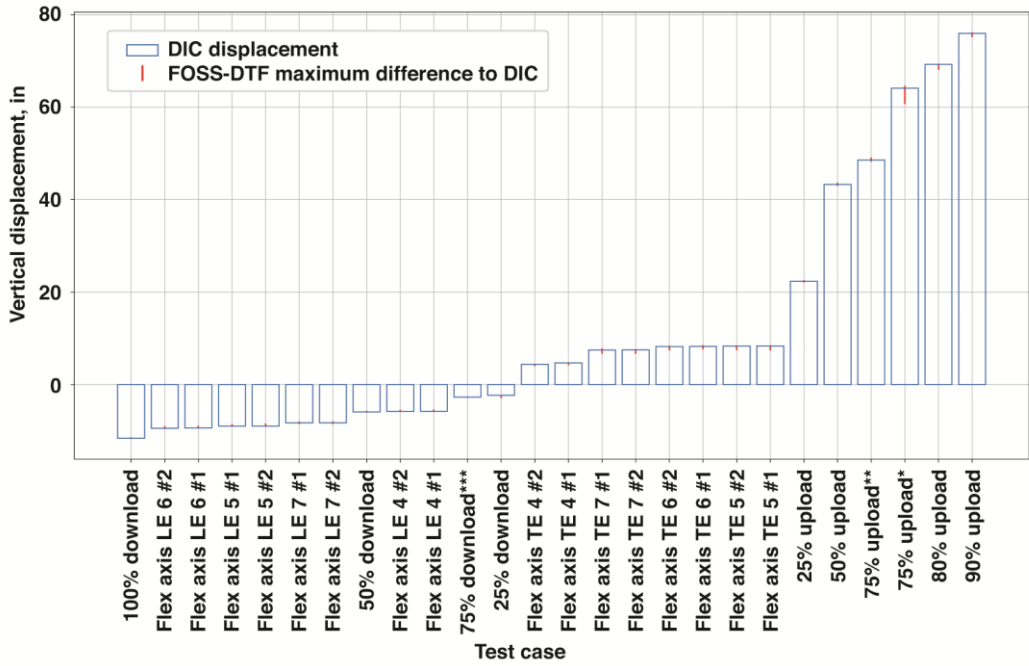
15

Figure 19. Wing-tip deflection summary, FOSS-DTF to DIC comparison.

Note (figure 19):
- * The test condition exceeded the FOSS operational strain range settings for the 75-percent Upload DLL test case.
- ** Data before exceeding the FOSS operational strain range settings for the 75-percent Upload DLL test case.
- *** Tip displacement not observed by DIC system due to test fixture obstruction; the next available target is presented.
- FOSS strain range settings reconfigured for 80-percent and 90-percent Upload test case.

Twist Transfer Function Test Results

The FOSS strain data recorded at the time of maximum wing-tip twist of 90-percent upload DLL are shown in figure 20. The 90-percent upload DLL is provided as the example load case because it has the largest wing-tip twist. The FOSS strain data shown in figure 20 and figure 21 were utilized with the rosette strain transformation equation (equation (13)) in order to determine shear strain at 13 stations along the wing span. The difference between the shear strain on the bottom surface and on the top surface was used in the TTF algorithm and is presented in figure 22.
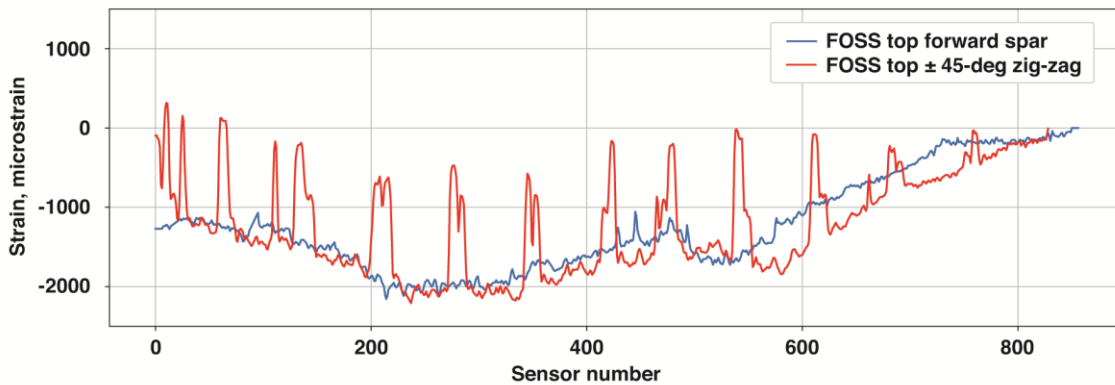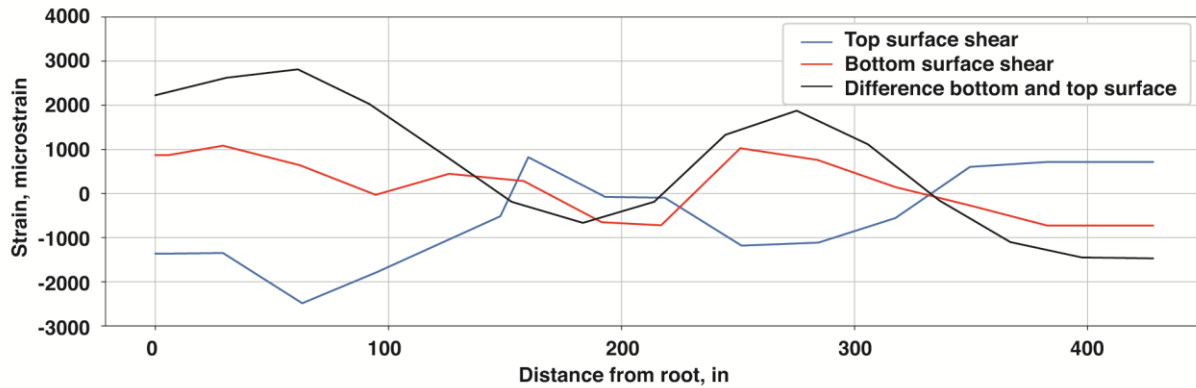

Figure 20. Load case 90-percent upload DLL FOSS strain distribution of top forward spar and top +/-45-deg pattern.

16
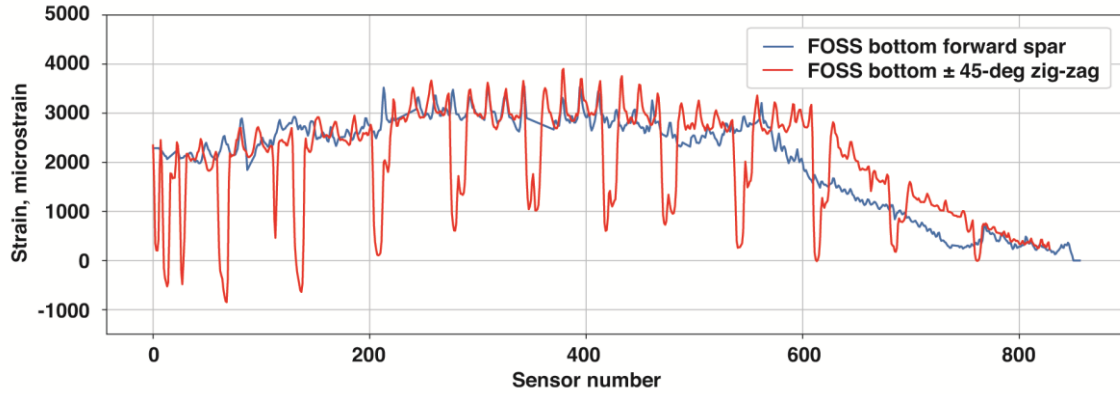
190187

Figure 21. Load case 90-percent upload DLL FOSS strain distribution of bottom forward spar and bottom +/-45-deg pattern.

190188

Figure 22. Load case 90-percent upload DLL FOSS shear-strain distribution on top surface (local coordinate frame).

Load cases Flex Axis 7 LE cycle #1 (upwards deflection) and Flex Axis 7 TE cycle #1 (downwards deflection) were used to determine the twist calibration term (C_{θ_k}) in equation (17). Improved results were obtained by using two separate twist-calibrations terms: one twist-calibration term for upwards loading, and a second for downwards loading. Root axial strains obtained by FOSS were used to determine the direction of bending for the selection of the twist-calibration term. The two different calibration terms may be due to non-symmetric torsional stiffness due to the construction of the wing structure where the skins, spars, and ribs are held together with fasteners as opposed to being bonded together. The two twist-calibration terms are presented in figure 23. The distributed shear strain, presented in figure 22 (the black curve), was then used with the calibration term for upwards loading (the blue curve) in figure 23 to calculate the elemental change in twist angle between sensing stations using equation (18).

17
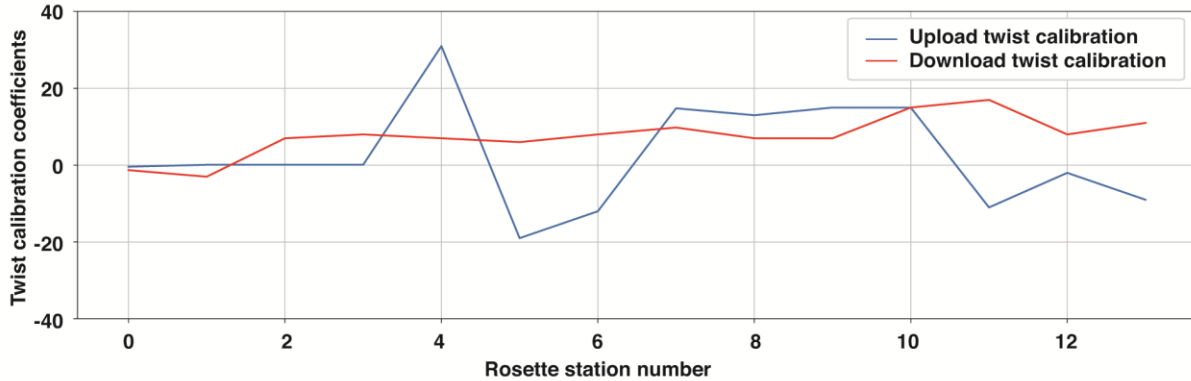
Figure 23. Twist calibration coefficients for upwards loading and downwards loading.

The twist-calibration term for uploading (see figure 23) and the distributed shear strain from 90-percent upload DLL (see figure 22) are processed with the TTF (eqs. (18) and (19)) to determine the FOSS-TTF distributed twist profile in the local coordinate frame aligned with the leading-edge spar. A spline-fitting interpolation filter was applied to the results to provide the same number of sensing stations as the distributed slope calculation in figure 15, and to increase the number of virtual shear-sensing stations. An equal number of sensing stations for twist and slope angle is required for a coordinate transformation into the global coordinate frame. The resulting local coordinate frame FOSS-TTF twist distribution plotted along with distributed inclinometers and the calculated twist from the DIC is presented in figure 24.
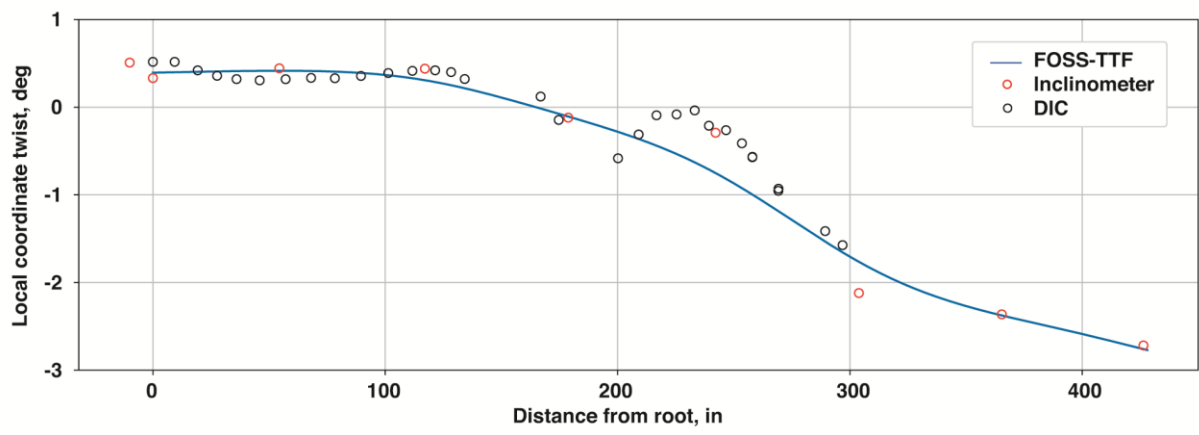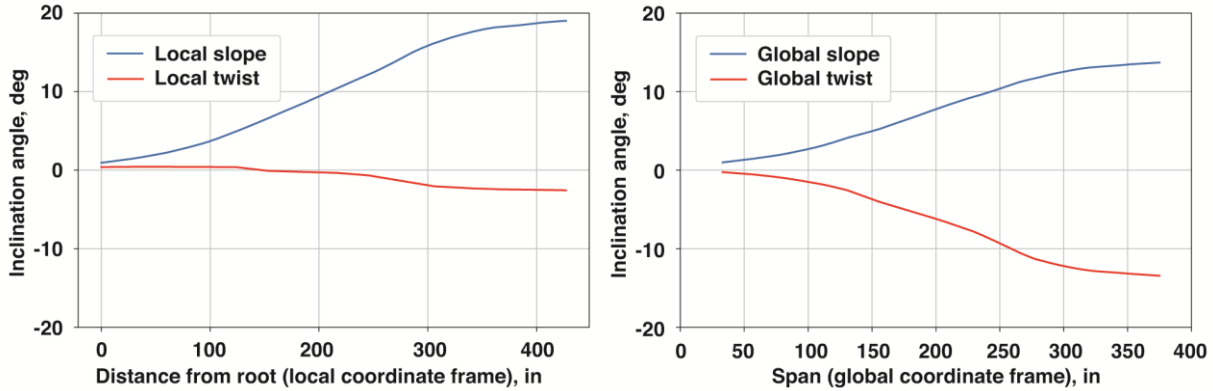

Figure 24. Load case 90-percent upload DLL twist distribution from FOSS-TTF, inclinometers and DIC (local coordinate frame).

In order to convert the slope and twist angle from the local coordinate frame into the global coordinate frame, the slope angles relative to the leading edge (ϕLE) and the twist angle relative to the leading edge (θLE) have to be rotated by the sweep angle of the leading edge (ΛLE). The rotation matrix is provided in equation (20). Wing-twist relative to the global coordinate frame is an important parameter to monitor because it represents a change in the local angle of attack of the airfoil relative to the incoming airflow. Increased angle of attack of an airfoil generally results in increased lift, assuming no flow separation. Airfoil drag is also affected by changes in the angle of attack.

18

$$\begin{bmatrix} \phi_g \\ \theta_g \end{bmatrix} = \begin{bmatrix} \cos(\Lambda_{LE}) & \sin(\Lambda_{LE}) \\ -\sin(\Lambda_{LE}) & \cos(\Lambda_{LE}) \end{bmatrix} \begin{bmatrix} \phi_{LE} \\ \theta_{LE} \end{bmatrix} \tag{20}$$

The slope angle and twist transformation from the local coordinate frame into the global coordinate frame is provided in figure 25. For the 90-percent upload DLL load case, the slope angle and the twist angle are both decreased when converted into the global coordinate frame.

Figure 25. Load case 90-percent upload DLL, distributed slope and twist angle transformed from local coordinate frame to global coordinate frame.
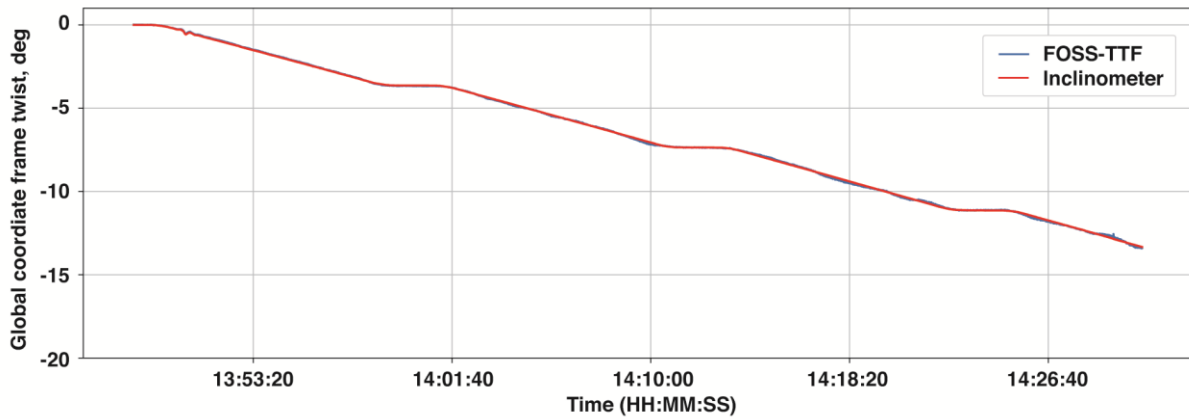
The resulting global coordinate frame twist distribution of the FOSS-TTF plotted along with distributed inclinometers and the calculated twist from the DIC is presented in figure 26. Due to the overhead loading system interfering with the view of wing-tip DIC targets (figure 10), the wing-tip DIC twist calculations were not obtained at the maximum load of 90-percent upload DLL. The FOSS-TTF therefore will only be compared against the inclinometers for the remainder of this report.
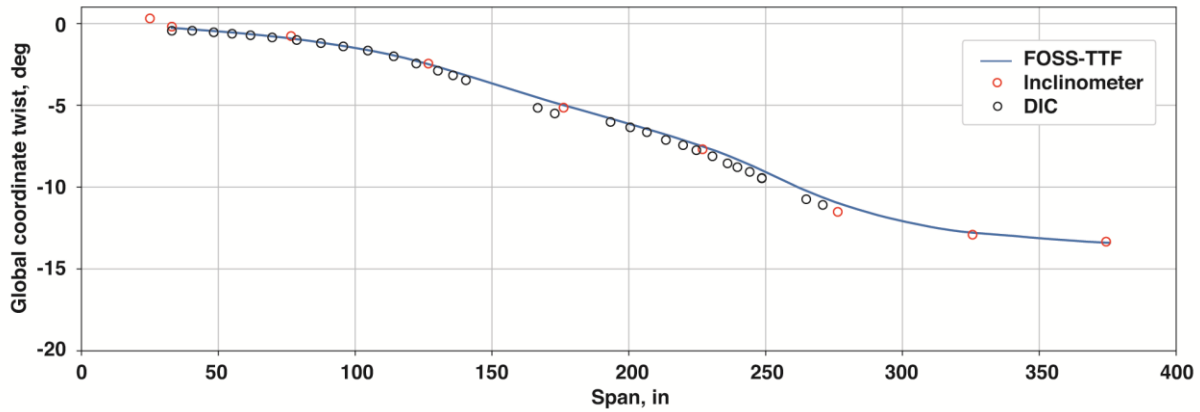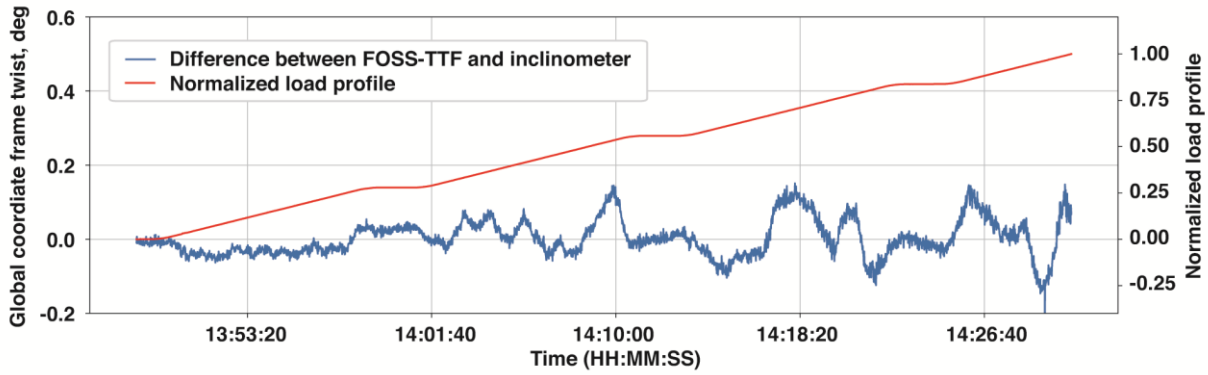

Figure 26. Load case 90-percent upload DLL, global coordinate twist distribution from FOSS-TTF, inclinometers, and DIC.

At the maximum twist, the inclinometer and FOSS-TTF were in close agreement with a difference of 0.07 deg, and a maximum difference over the time profile of 0.29 deg. The inclinometer recorded a maximum twist of -13.33 deg at the wing tip and the FOSS-TTF recorded -13.40 deg. The time history of the inclinometer and FOSS-TTF wing-tip twist for Load case 90-percent upload DLL is shown in figure 27. The time history of the difference between FOSS-TTF and inclinometer is shown in figure 28.

19

Figure 27. Load case 90-percent upload DLL wing global coordinate frame tip twist time history, FOSS-TTF and inclinometer.

Figure 28. Load case 90-percent upload DLL time history of difference in wing-tip twist between FOSS-TTF and inclinometer.

The mean difference from the FOSS-TTF and inclinometer for Load case 90-percent upload DLL is 0.003 deg, the standard deviation is 0.05 deg, and the maximum deviation is 0.29 deg out of 13.33 deg.

A summary of the remaining load cases is shown in figure 29. Over all the load case profiles, the maximum difference between the inclinometer and FOSS-TTF wing-tip twist in the global coordinate frame is 0.43 deg for the 25-percent download DLL case.
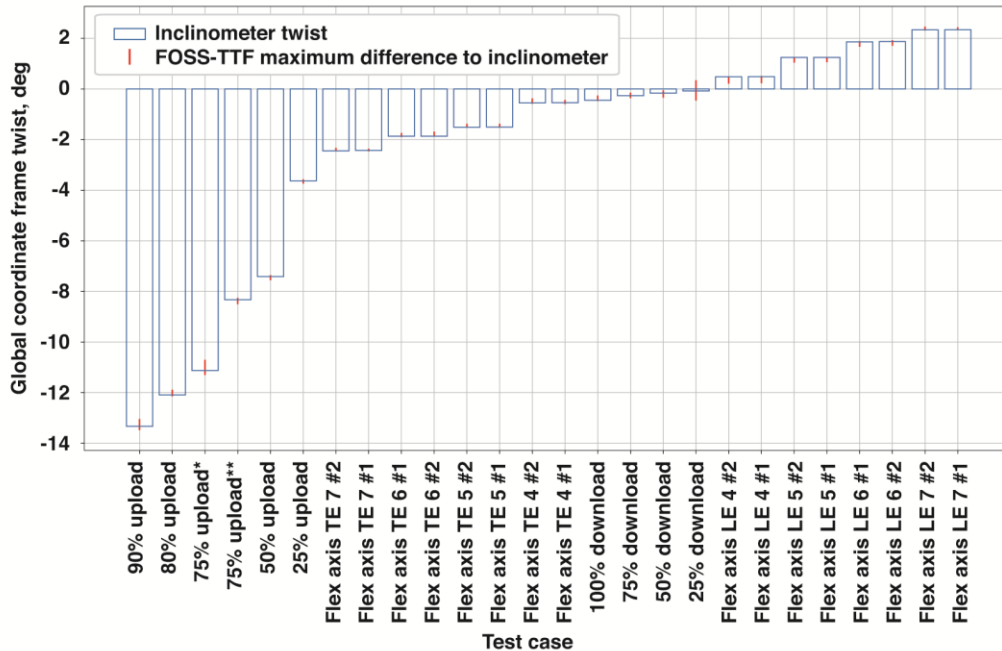
Figure 29. Wing-tip twist summary, FOSS-TTF to inclinometer comparison.

Note (figure 29):
-    * The test condition exceeded the FOSS operational strain range settings for the 75-percent Upload test case.
-    ** Data before exceeding the FOSS operational strain range settings for the 75-percent Upload test case.
-    FOSS strain range settings reconfigured for 80-percent and 90-percent Upload test case.

Conclusion

The algorithms presented in this paper demonstrate the ability to effectively use distributed strain measurements to determine wing deflection and twist on high-aspect-ratio, swept-wing structures. Both the Displacement Transfer Function (FOSS-DTF) and Twist Transfer Function (FOSS-TTF) were shown to accurately estimate the deformation of the Passive Aeroelastic Tailored wing (PAT wing) when calibrated and paired with the NASA Armstrong Flight Research Center (AFRC) Fiber Optic Sensing System (FOSS). At the maximum vertical deflection of 75.99 inches, the Digital Image Correlation (DIC) system and FOSS-DTF were in close agreement with a maximum difference of 0.6 percent, and the string potentiometer and FOSS-DTF were in close agreement with a maximum difference of 2.2 percent. At the maximum wing twist of -13.33 deg, the inclinometer and FOSS-TTF were within 0.5 percent. The DIC twist measurements were intermittently available due to the overhead loading system obstructing the stereoscopic camera system view of DIC targets throughout the loading cycles.

The results presented also demonstrate the ability to easily implement these algorithms for use in flight for both health monitoring and control applications. The potential integration of the AFRC FOSS for structural monitoring of aircraft could allow reduction of weight while maintaining a high level of confidence in future aircraft designs. In addition, a real-time monitoring system can reduce the risk of in-flight structural failure by providing crucial flight data including wing deformations and structural stresses.

Traditional sensing instrumentation including metallic foil strain gages, accelerometers, and thermocouples tend to be heavy and bulky, limiting their application to a few sensors, usually near the wing root. Recent improvements in fiber-optic technology have enabled the use of slim surface-mounted fiber Bragg gratings, which provide numerous distributed strain and temperature measurements from a variety of structural elements. Because of their accuracy, light weight, small size, and flexibility, these fiber-optic sensors are ideal for flying aircraft having strict weight and size limitations. The use of the

FOSS along with the displacement and twist transfer functions could also be used to control of the shape of a wing structure during flight, potentially preventing aeroelastic divergence.

References

1. Noll, Thomas E., et al., "Technical Findings, Lessons Learned, and Recommendations Resulting from the Helios Prototype Vehicle Mishap," presented at the NATO/RTO AVT-145 Workshop on Design Concepts, Processes, and Criteria for UAV Structural Integrity, Florence, Italy, May 14-18, 2007.

2. DeAngelis, V. Michael, and Robert Fodale, "Electro-Optical Flight Deflection Measurement System," in *Society of Flight Test Engineers,* 1987, pp. 22-1 to 22-14.

3. DeAngelis, V. M., "In-Flight Deflection Measurement of the HiMAT Aeroelastically Tailored Wing," AIAA-81-2450, 1981.

4. Lokos, William A., "Predicted and Measured In-Flight Wing Deformations of a Forward-Swept-Wing Aircraft," in *Society of Flight Test Engineers,* 1990, pp. 3.1-1 to 3.1-20.

5. Bonnema, Kenneth L., and William A. Lokos, "AFTI/F-111 Mission Adaptive Wing Flight Test Instrumentation Overview," in *Proceedings of the 35th International Instrumentation Symposium,* 1989, pp. 809-840.

6. Lokos, William A., Catherine M. Bahm, and Robert A. Heinle, *Determination of Stores Pointing Error Due to Wing Flexibility Under Flight Load*, NASA TM-4646, December 1994.

7. Lizotte, Andrew M., and William A. Lokos, *Deflection-Based Structural Loads Estimation From the Active Aeroelastice Wing F/A-18 Aircraft,* NASA/TM-2005-212871, May 2005.

8. Richards, W. Lance, Allen R. Parker, William L. Ko, Anthony Piazza, and Patrick Chan, "Application of Fiber Optic Instrumentation," RTO AGARDograph 160, 2012.

9. Jutte, Christine V., William L. Ko, Craig A. Stephens, John A. Bakalyar, W. Lance Richards, and Allen R. Parker, *Deformed Shape Calculation of a Full-Scale Wing Using Fiber Optic Strain Data from a Ground Loads Test,* NASA/TP-2011-215975, December 2011.

10. Ryan, John J., John T. Bosworth, John J. Burken, and Peter M. Suh, "Current and Future Research in Active Control of Lightweight, Flexible Structures Using the X-56 Aircraft," AIAA-2014-0597, 2014.

11. Pena, Francisco, Benjamin L. Martins, and W. Lance Richards, *Active In-flight Load Redistribution Utilizing Fiber-Optic Shape Sensing and Multiple Control Surfaces,* NASA/TM-2018-219741, February 2018.

12. Budynas, Richard G., and J. Keith Nisbett, *Shigley's Mechanical Engineering Design, Eighth Edition,* McGraw Hill, New York, 2008.

13. Bakalyar, John, and Christine Jutte, "Validation Tests of Fiber Optic Strain-Based Operational Shape and Load Measurements, AIAA-2012-1904, 2012.

14. Ko, William L., Richards, William. L, and Tran, Van T., *Displacement Theories for In-Flight Deformed Shape Predictions of Aerospace Structures,* NASA/TP-2007-214612, January 2007.